A Fundamental Assessment of the Concept of Mean Beam Length for Application for Multi-dimensional Non-Gray Radiative Heat Transfer

By

Walter W. Yuen
Department of Mechanical Engineering
Santa Clara University
500 El Camino Real
Santa Barbara, California, 95053
Tel: 805-403-3637
Email: wwyuen@scu.edu

Wai Cheong Tam
Fire Research Division
National Institute of Standards and Technology
100 Bureau Drive
Gaithersburg, Maryland, USA
Tel: 301-975-8202
Email: waicheong.tam@nist.gov

Abstract

The traditional concept of mean beam length (MBL) and its recommended empirical expression are demonstrated to be inaccurate for general application for the evaluation of multi-dimensional non-gray radiative heat transfer. A new concept, namely Point Mean Beam Length (PMBL), is proposed and the formulation of PMBL is provided. The mathematical properties of PMBL for three common geometries including sphere, cylinder, and slab are presented. Results show that PMBL is more effective in generating an accurate evaluation of radiative heat transfer from a differential area to any finite area at the boundary of an enclosure with an isothermal absorbing/emitting medium. The deficiency of the traditional mean beam length empirical expression is illustrated. A concept of "optimal" point mean beam length (OPMBL) is demonstrated to be a more accurate length scale for practical applications. In contrast to the traditional MBL, a single value of OPMBL is applicable for all gas absorption bands, independent of the strength and shape of the absorption bands. The proposed work provide a mathematically validated approach to efficiently and accurately evaluate the radiation heat transfer within an isothermal, non-gray, multi-dimensional medium.

Keywords: radiation heat transfer, point mean beam length, optimal mean beam length, multi-dimensional, nongray medium.

1. Introduction

Radiative heat transfer is an important and often the dominant mode of heat transfer in many high-temperature industrial applications such as furnaces, boilers, gas turbines, and high-temperature fibrous thermal protection systems. Accurate engineering analysis of these systems requires solutions to the radiative transfer equation (RTE) in systems with multi-dimensional geometry, non-gray radiative properties, and inhomogeneous spatial distribution in temperature and species concentration. Over the years, a significant amount of effort has been made to develop accurate solutions to the RTE. Since the geometric effect of radiative heat transfer and the spectral effect of the absorption properties of the medium are treated independently by the RTE, much of the research is focused on the two effects separately. For example, different solution methods, such as the Zonal Method [1-3], Discrete Ordinate Method [4,5], Finite Volume Method [6], P-N (Spherical Harmonics) method [7,8], natural element method [9], and Monte Carlo Method [10-12] have been developed to address the multi-dimensional effect. They have been demonstrated to be effective for multi-dimensional radiative heat transfer in a gray medium. Different spectral models, such as the various narrow-band models [13-15], the k-distribution (and correlated k-distribution) method [16-17], and the weighted gray gas models [18-20] have been developed to address the highly complex non-gray spectral absorption behavior of combustion gases. Some of these models have been verified to be accurate by comparison with line-by-line direct integration [21,22] and demonstrated to be effective in evaluating the total absorptivity/emissivity of nongray mediums such as combustion gases in a one-dimensional system.

For the evaluation of multi-dimensional radiative heat transfer in a nongray system, however, the progress of the research is limited. Many attempts to develop solutions to multi-dimensional radiative transfer in a nongray isothermal medium by combining the different solution methods with the different spectral models have been reported in the literature [23-27]. While these efforts are valuable in providing benchmark solutions, particularly in assessing the accuracy of approximate solutions, the approaches are still too computationally intensive to be implemented by the practical engineering community. For example, in transient analysis of non-gray radiative heat transfer in a rectangular enclosure with an isothermal combustion gas using the zonal method and a narrow-band model with a 10 x 10 x 10 grid nodalization, to update the radiative heat transfer between the differential volume and area zones numerically (without any approximation) would require over 400 million numerical integrations at every time step, as the temperature and the species concentration of the medium are changing with time [28,29]. Similar computational efforts are required using other solution methods (e.g. Monte Carlo, Discrete Ordinate Method) and spectral models (e.g. k-distribution and line-by-line integration). Simplification and/or approximations are required if the assessment of radiative heat transfer is needed in the design of practical engineering systems.

Over the years, many approximate approaches have been reported to address the mathematical complexity of multi-dimensional radiative heat transfer in nongray systems. Few of them, however, have made sufficient progress to be accepted broadly by the industry. Currently, the most commonly accepted approximate approach for multi-dimensional nongray radiative heat transfer is to utilize the concept of mean beam length (MBL). Introduced by Hottel [1] and studied by many researchers [30-34] over the years, the MBL is used as a length scale so that the one-dimensional results can be used to approximate the total absorptivity/emissivity for radiative exchange between a three-dimensional volume and its total boundary. The MBL concept was only being verified to be used in predicting the total emissivity of combustion gases in enclosures with simple geometry (e.g. sphere, cube) [30-34]. An empirical expression for the MBL (4*C*V/A, with C being the correction factor ,and V and A being the volume and boundary area of the enclosure) was introduced for enclosures with arbitrary three-dimensional geometries. In recent years, the concept of MBL is also used to generate approximate solutions for multi-dimensional nongray radiative heat transfer in a non-isothermal inhomogeneous medium. Specifically, a local absorption coefficient for a computational cell is generated by the one-dimensional total emissivity using MBL ($4*C*V_c/A_c$ with V_c and A_c being the volume and boundary of the computational cell) and the local radiative properties of the medium, thus accounting for the nonisothermal and inhomogeneous effect. The local absorption coefficient is then used in the full computation with a particular radiation solver. Results using this approach have appeared in the literature [35,36] and this approach has also adopted by some CFD codes (e.g. FLUENT, CFAST, FDS) [37-39] as an option for the user to simulate the radiative heat transfer effect.

However, due to the lack of numerically efficient and accurate calculation methods, the MBL approach has been used as an approximation. In the fire research community, the MBL is often being used to evaluate the localized effect of radiation heat transfer [40,41]. Yet, the use of MBL has not been validated for the evaluation of local radiative heat transfer, even for an isothermal medium in enclosures with simple geometry (e.g. cylinder, cube). For a design calculation using a CFD code, while the use of the MBL concept in the evaluation of the local absorption coefficient in a computational cell is physically reasonable, the accuracy of this approach has also not been rigorously verified. Therefore, results generated by such computations thus have uncertain accuracy and improvements are needed in the computation of radiative heat transfer in non-gray multi-dimensional systems.

Given the fact that the MBL concept is a key component in implementing the non-gray multi-dimensional applications, the objective of this work, together with results presented in reference [42], is to systematically assess the accuracy of the traditional MBL approach and to develop modifications of the concept which can extend the accuracy of its implementation in enclosures with different geometries. Specifically, a concept of point mean beam length (PMBL), is introduced. In contrast to the traditional MBL, PMBL is defined as the length scale for the radiative heat transfer between a differential area and a finite area with an intervening absorbing/emitting medium. In general, the traditional MBL can be generated from PMBL by an integration over the emitting area. While PMBL is still a function of wavelength, the effect on the differential exchange factor due to the spectral variation of PMBL is not strong and an “optimal” PMBL (OPMBL) can be identified as a constant length scale for the evaluation of the radiative heat transfer over the whole range of optical thickness. As illustrations, PMBL is implemented with the zonal method to generate accurate and computationally efficient solutions to radiative heat transfer in some two-dimensional and three-dimensional enclosures. These solutions will be valuable for benchmark purposes.

In reference [42], results are presented for radiative exchange between rectangular surfaces in various parallel and perpendicular configurations, which are important for the analysis of non-gray radiative heat transfer in a rectangular enclosure. In the present work, the accuracy and mathematical properties of the PMBL concept for three general 3D and

2D geometries (sphere, cylinder, and slab) are further investigated. The limitation of the traditional MBL in these 3D and 2D enclosures is illustrated by comparison with the OPMBL results.

2. The concept of point mean beam length (PMBL)

For a diffusely emitting area dA_1 and a second finite area A_2, the differential exchange factor for radiative transfer is given by

$$ds_1s_2 = dA_1 \int_{A_2} \frac{cos\theta_1 cos\theta_2}{\pi L^2} e^{-aL} dA_2 \tag{1}$$

where θ_i $(i = 1,2)$ is the angle between the unit surface normal at the two differential surface dA_i $(i = 1, 2)$ and the line of sight between the two differential surfaces. L is the length of the line of sight and a is the absorption coefficient of the intervening medium. A point mean beam length, L_{pmb}, is defined to be the equivalent length scale such that the geometrical mean transmittance between the differential area dA_1 and the finite area A_2, τ_{d1-2}, can be written in a one-dimensional form as

$$\tau_{d1-2} = \frac{d\,s_1s_2}{dA_1 F_{d1-2}} = e^{-aL_{pmb}} \tag{2}$$

where the differential view factor, F_{d1-2} is defined by

$$F_{d1-2} = \int_{A_2} \frac{cos\theta_1 cos\theta_2}{\pi L^2} dA_2 \tag{3}$$

Eq. (1) can be integrated over the emitting area A_1 to yield the exchange factor between the two finite areas

$$s_1s_2 = \int_{A_1} \int_{A_2} \frac{cos\theta_1 cos\theta_2}{\pi L^2} e^{-aL} dA_2\, dA_1 \tag{4}$$

The traditional mean beam length, MBL, for the two finite areas A_1 and A_2 is defined as

$$\tau_{1-2} = \frac{s_1s_2}{A_1F_{1-2}} = e^{-aL_{mb}} \tag{5}$$

with F_{1-2} being the view factor given by

$$F_{1-2} = \int_{A_1} \int_{A_2} \frac{cos\,\theta_1 cos\theta_2}{\pi L^2} dA_2 dA_1$$

A comparison between Eqs. (2) and (5) yields the following relation between PMBL and MBL,

$$e^{-aL_{mb}} = \frac{1}{A_1F_{1-2}} \int_{A_1} F_{d1-2} e^{-aL_{pmb}}\, dA_1 \tag{6}$$

It should be noted that for a general enclosure, PMBL is defined for a local differential area and is generally not the same as the traditional MBL. For enclosures with geometrical symmetry such as a sphere, infinite cylinder, and slab, PMBL and MBL are identical when the emitting surface A_1 and the absorbing surface A_2 are the total bounding surface of the enclosure since PMBL is identical at every point of the emitting surface A_1 due to symmetry. To further understand its mathematical behavior, the PMBL for three simple geometrical configurations (sphere, cylinder, and slab) are presented in the following sections.

2.1 Sphere

Using the coordinate system as shown in Fig. 1, Eq. (1) becomes (see Appendix for detail)

$$ds_1 ds_2 = \frac{R^2(1+cos\theta)^2}{\pi L^4} e^{-aL} dA_1 dA_2 \tag{7}$$

Consider A_2 as the upper portion of the spherical surface (i.e. a spherical cap with $0 < \theta < \theta_c$), Eq. (7) can be integrated to yield (see Appendix for the detail)

$$\frac{ds_1 s_2}{dA_1} = -\frac{1}{2aR}\left[2e^{-2aR} - \sqrt{2(cos\theta_c + 1)}e^{-\sqrt{2(cos\theta_c+1)}aR}\right] + \frac{1}{2(aR)^2}\left(e^{-\sqrt{2(cos\theta_c+1)}aR} - e^{-2aR}\right) \tag{8}$$

The view factor is given by

$$F_{d1-2} = \frac{1}{2}[1 - cos\theta_c] \tag{9}$$

and based on Eq. (2), the PMBL is

$$\frac{L_{pmb}}{R} = -\frac{1}{aR[1-cos\theta_c]} ln\left[2e^{-2aR} - \sqrt{2(cos\theta_c + 1)}e^{-\sqrt{2(cos\theta_c+1)}aR} + \frac{1}{aR}\left(e^{-\sqrt{2(cos\theta_c+1)}aR} - e^{-2aR}\right)\right] \tag{10}$$

In the optically thin limit ($aR \to 0$), the PMBL becomes

$$\frac{L_{pmb,0}}{R} = \frac{\frac{8}{3} - \frac{1}{3}[2(cos\theta_c + 1)]^{\frac{3}{2}}}{1 - cos\theta_c} \tag{11}$$

In the limit of A_2 being the whole spherical surface ($\theta_c = \pi$), Eqs. (8), (10) and (11) are identical to those presented in a separate publication [42]. The PMBL for an absorbing area A_2 with different values of θ_c are presented as functions of optical thickness aR in Fig. 2.

Numerically, it can be shown that from the perspective of the evaluation of the exchange factor ($ds_1 s_2$ at a specific wavelength), the effect of the variation of PMBL with optical thickness is generally not strong and a constant length scale can be selected to generate an accurate approximation to the exchange factor over all wavelengths. To give this length scale a precise mathematical definition, a concept of "optimal" point mean beam length (OPMBL) is introduced. Specifically, for a length scale L, the error between the actual exchange factor and the approximate value generated by L for a specific absorption coefficient can be written as

$$E(L) = \left|\frac{ds_1s_2}{dA_1} - F_{d1-2}e^{-aR\left(\frac{L}{R}\right)}\right| \tag{12a}$$

To assess the overall error of the approximation, an average sum of the square of the error is evaluated to be

$$S(L) = \frac{1}{(aR)_{0.01}}\int_0^{(aR)_{0.01}} E(L)^2\, d(aR) \tag{12b}$$

The upper limit of the integration in Eq. (12b), $(aR)_{0.01}$, is taken to be the optical thickness at which the geometric mean transmittance (τ_{d1-2}) is 0.01 because beyond this optical thickness, both the approximate and exact expression of the transmissivity is close to zero and the value of *E(L)* is negligibly small and insignificant. The length scale which has the minimum value of *S(L)* is identified as the OPMBL. The values of OPMBL for the absorbing area with different θ_c are identified as single points at the various PMBL curves in Fig. 2. The overall effect of geometry (θ_c) on OPMBL is illustrated by Fig. 3. It is interesting to note that the value of the traditional mean beam length (1.2R, correspond to the value of 3.6V/A for a sphere) agrees well with the OPMBL when the absorbing area, A_2, is the whole spherical surface ($\theta_c = \pi$).

To illustrate the accuracy of using OPMBL and also the deficiency of the traditional MBL in generating accurate approximations, the exchange factor generated by the OPMBL ($s_1s_2 = A_1F_{12}\exp\left(-aL_{pmb,o}\right)$) together with the approximate exchange factor generated by the traditional MBL ($s_1s_2 = A_1F_{12}\exp\left(-1.2aR\right)$) are compared with the exact solution (a direct integration of Eq.(4) at a specific optical thickness) with A_2 being a hemispherical surface with $\theta_c = \pi/2$. The results are shown in Fig. 4. The agreement between the OPMBL approximation and the exact solution is excellent with negligible error (< 0.01) as lines representing the two solutions are practically indistinguishable in the figure. The error of the approximation of using the traditional MBL, on the other hand, is quite large with a maximum absolute error greater than 0.06. The corresponding relative error in the region of optical thickness with the maximum absolute error is quite large. For example, with $aR = 1.0$, both the exact and PMBL solution for the exchange factor, s_1s_2, is 0.09. The value predicted by MBL expression ($s_1s_2 = A_1F_{12}\exp\left(-1.2aR\right)$), on the other hand, is 0.15. The relative error is 67%.

Over the years, many researchers have made efforts to identify different MBL's for different gas absorption bands [30-34]. For a spherical enclosure [30,34], for example, the traditional MBL for a weakly absorbing band was established to be $4R/3$, which is equivalent to the optically thin limit of L_{pmb} for the whole spherical surface, as shown in Fig. 2. The traditional MBL for a strongly absorbing band (the square-root limit) was determined to be *6R/5*, which is close to the value of OPMBL. Physically, an absorption band is the summation of individual absorption lines that follow the exponential attenuation behavior of radiative absorption. Since OPMBL is demonstrated to be effective in generating an accurate approximation to the exchange factor over the whole range of the absorption coefficient with exponential attenuation, it is applicable for all absorption bands, independent of the strength (i.e. the optical thickness) and the shape of the absorption bands. The selection of a specific quantitative definition of OPMBL (based on Eqs. (12a) and (12b)) and the approximation used in the development of the different gas absorption band models are the reasons for the slight difference between OPMBL and the different traditional MBL's recommended for the different bands.

2.2 Cylinder

For an infinite cylinder, Fig. 1, interpreted as a two-dimensional planar system, can still be used as the geometry and coordinate system for mathematical development. Based on the mathematical development presented in the Appendix, the exchange factor between the two differential area dA_1 and dA_2 is given by

$$\frac{ds_1 ds_2}{dA_1} = S_3(2aRcos\beta)cos\beta d\beta \tag{14}$$

where $S_3(x)$ is the two-dimensional radiation function given by [43]

$$S_3(x) = \frac{2}{\pi}\int_1^{\infty}\frac{e^{-xt}}{t^3\,(t^2-1)^{1/2}}dt \tag{15}$$

Numerical values for $S_3(x)$ are tabulated and available in reference [43]. Note that for the two-dimensional planar system, dA_1 and dA_2 are infinitesimal strips of infinite length in the direction perpendicular to the two-dimensional x-z plane.

For an angular section extending from $\theta = 0$ to $\theta = \theta_c$, equation (14) can be integrated to yield the exchange factor

$$\frac{ds_1 s_2}{dA_1} = \int_0^{\frac{\theta_c}{2}} S_3(2aRcos\beta)cos\beta d\beta \tag{16}$$

The view factor is

$$F_{d1-2} = \frac{ds_1 s_2}{dA_1}(aR = 0) = \frac{1}{2}sin\frac{\theta_c}{2} \tag{17}$$

and the PMBL is given by

$$\frac{L_{pmb}}{R} = -\frac{1}{aR}ln\left[\frac{2}{sin\frac{\theta_c}{2}}\int_0^{\frac{\theta_c}{2}} S_3(2aRcos\beta)cos\beta d\beta\right] \tag{18}$$

In the optically thin limit $(aR \to 0)$, the PMBL is reduced to

$$\frac{L_{pmb,0}}{R} = \frac{4}{\pi}\left[\frac{\frac{\theta_c}{2}+\frac{1}{2}sin\theta_c}{sin\frac{\theta_c}{2}}\right] \tag{19}$$

The PMBL for different absorbing circular sections with different values of θ_c is shown in Fig. 5. The corresponding OPMBL are identified in the same figure and also presented as a function of θ_c in Fig. 6. Similar to a spherical enclosure, the OPMBL for the whole cylindrical surface (*1.707R*) agrees well with the traditional MBL value of *1.8R*, as well as the traditional MBL evaluated for different gas absorption bands [34]. It is interesting to note that the PMBL (and OPMBL) in some cases can be greater than the diameter (2R) of the cylindrical enclosure. Physically, the radiative exchange between two areas in a two-dimensional cylindrical surface includes the radiative exchange between differential areas outside of the two-dimensional plane for which the line-of-sight length scale is greater than the diameter of the two-dimensional circular cross-section. The PMBL (and OPMBL) can thus be greater than the diameter of the circular cross-section. The traditional MBL cannot account for this important physical effect.

The effectiveness of the OPMBL and the deficiency of the traditional MBL in generating approximations to the differential exchange factor is demonstrated in Fig. 7 for the half-circular upper section ($\theta_c = \pi/2$). The error of the traditional MBL is substantial with a relative error of more than 40% in the region of moderate optical thickness.

Using the principle of superposition, the OPMBL results generated for the upper circular section of the surface can be used to generate the exchange factor between two arbitrary circular arcs with geometry as shown in Fig. 8. The exchange factor can be written as a single integration as

$$s_1s_2 = \int_{A_1}\begin{bmatrix} F_{d1-2U}(\theta_{d1-2U})e^{-aL_{pmb,o}(\theta_{d1-2U})} \\ -F_{d1-2L}(\theta_{d1-2L})e^{-aL_{pmb,o}(\theta_{d1-2L})} \end{bmatrix}dA_1 \tag{20}$$

where θ_{d1-2U} and θ_{d1-2L} are the angular coordinates at the lower and upper edge of A_2 relative to dA_1 as shown in Fig. 8. Since OPMBL is independent of the absorption coefficient, this procedure can be used to generate the radiative heat transfer between the two circular arcs with any absorbing non-gray medium with known spectral absorption characteristics. Solutions for a CO_2/H_2O/soot mixture using RADNNET [44] as the spectral solver are currently under consideration and the computer code will be made available to the community in future publications.

2.3 Slab

For an infinite two-dimensional slab, the radiative exchange is considered for two cases with dA_1 is either parallel or perpendicular to the absorbing surface as shown in Figs. 9a and 9b. The differential exchange factor for the case with parallel dA_1 (Fig. 9a) is given by (see Appendix for the detailed derivation)

$$\left[\frac{ds_1s_2}{dA_1}\right]_{pp} = \int_0^{L/D}\frac{1}{(\eta^2+1)^{\frac{3}{2}}}S_3\left[aD\sqrt{\eta^2+1}\right]d\eta \tag{21}$$

with $\eta = x/D$. The two length scales, L and D, correspond to the width of the finite area A_2 and the distance between dA_1 and A_2, as shown in Fig. 9a. The view factor is

$$[F_{d1-2}]_{pp} = \left[\frac{ds_1s_2}{dA_1}\right]_{pp}(aD = 0) = \frac{1}{2}\frac{L}{\sqrt{L^2+D^2}} \tag{22}$$

The PMBL is

$$\frac{L_{pmb,pp}}{D} = -\frac{1}{aD}ln\left[2\sqrt{1+\frac{D^2}{L^2}}\int_0^{L/D}\frac{1}{(\eta^2+1)^{\frac{3}{2}}}S_3\left[aD\sqrt{\eta^2+1}\right]d\eta\right] \tag{23}$$

In the optically thin limit ($aD \rightarrow 0$),

$$\frac{L_{pmb,pp,0}}{D} = \frac{4}{\pi}\frac{\sqrt{L^2+D^2}}{L}tan^{-1}\frac{L}{D} \tag{24}$$

The corresponding expressions for the case with a perpendicular dA_1, with the geometry as shown in Fig. 9b, are

$$\left[\frac{ds_1s_2}{dA_1}\right]_{pd} = \int_0^{L/D}\frac{\eta}{(\eta^2+1)^{\frac{3}{2}}}S_3\left[aD\sqrt{\eta^2+1}\right]d\eta \tag{25}$$

$$[F_{d1-2}]_{pd} = \left[\frac{ds_1s_2}{dA_1}\right]_{pd}(aD = 0) = \frac{1}{2}\left(1-\frac{D}{\sqrt{L^2+D^2}}\right) \tag{26}$$

$$\frac{L_{pmb,pd}}{D} = -\frac{1}{aD}ln\left[2\frac{\sqrt{D^2+L^2}}{\sqrt{D^2+L^2}-D}\int_0^{L/D}\frac{\eta}{(\eta^2+1)^{\frac{3}{2}}}S_3\left[aD\sqrt{\eta^2+1}\right]d\eta\right] \tag{27}$$

$$\frac{L_{pmb,pd,0}}{D} = \frac{2}{\pi}\frac{\sqrt{D^2+L^2}}{\sqrt{D^2+L^2}-D}\ ln\left(1+\frac{L^2}{D^2}\right) \tag{28}$$

The PMBL for the two different orientations of dA_1 is presented in Figs. 10a and 10b. The corresponding OPMBL is shown in Fig. 11. It is interesting to note that the value of OPMBL differs significantly from the traditional MBL of 1.8D for both cases. The OPMBL with a perpendicular dA_1, $L_{pmb,pd,o}$, is generally greater than the OPMBL with a parallel dA_1, $L_{pmb,pp,o}$ (more than a factor of 2 in the region of large optical thickness). Physically, the energy emitted from a perpendicular dA_1 can penetrate much further along the upper surface than energy emitted from a parallel dA_1. This accounts for the large increase in the PMBL and OPMBL.

The error of the traditional MBL is illustrated in Figs. 12a and 12b for an upper surface with L/D = 5 (close to the infinite slab for the parallel case). While the approximate exchange factor with OPMBL agrees well with the exact solution, the approximate exchange factor generated with the traditional MBL has significant errors (with a maximum absolute error of 0.03 and a relative error of more than 30% in the region of moderate optical thickness).

For two-dimensional finite areas as shown in Figs. 13a and 13b, the exchange factor can be generated using the OPMBL results by superposition as follow

$$[s_1 s_2]_{pp} = \int_{A_1} \begin{bmatrix} F_{d1-2U,pp}\big((L_U - x)/D\big)e^{-aL_{pmb,pp,o}(L_U/D)} \\ -F_{d1-2L,pp}\big((L_L - x)/D\big)e^{-aL_{pmb,pp,o}(L_L/D)} \end{bmatrix} dA_1 \qquad (20a)$$

for the case with two parallel areas (Fig. 13a), and

$$[s_1 s_2]_{pd} = \int_{A_1} \begin{bmatrix} F_{d1-2U,pd}\big(L_U/(D-z)\big)e^{-aL_{pmb,pd,o}(L_U/(D-z))} \\ -F_{d1-2L,pd}\big(L_L/(D-z)\big)e^{-aL_{pmb,pd,o}(L_L/(D-z))} \end{bmatrix} dA_1 \qquad (20b)$$

for the case with two perpendicular areas (Fig. 13b). Similar to the 3D total exchange factors developed for rectangular areas [42], Eqs. (20a) and (20b) can be considered as fundamental solutions for general 2D non-gray radiative heat transfer using superposition with a specific spectral radiation solver. Using RADNNET [44] as the spectral solver, these solutions are currently being developed and computer software will be made available to the community in future publications.

3. Conclusion

A new concept of point mean beam length (PMBL) is presented. Numerical results for PMBL are generated for three specific geometries (sphere, cylinder, and parallel slab). For all three geometries, the effect of the variation of PMBL with the optical thickness on the evaluation of the exchange factor is not strong and a constant length scale can be used to generate an accurate evaluation of the exchange factor over the full range of optical thicknesses. An "optimal" point mean beam length (OPMBL) is identified as the appropriate length scale.

For radiative exchange between the full bounding surface and itself in enclosures with simple geometries (sphere, cylinder, and parallel slab), the OPMBL and the traditional MBL (*3.6V/A*) are approximately equal. The two concepts, therefore, are equally effective in predicting the non-gray exchange factor for those cases. But for radiative exchange between different parts of the enclosed surface, results generated by the traditional MBL have significant errors, while results generated by the OPMBL approach agree well with exact solutions.

For enclosures with simple geometries (sphere, cylinder, and parallel slab), analytical expressions for OPMBL for a part of the bounding surface are developed and numerical solutions are presented. For a two-dimensional infinite cylinder and parallel slab, these OPMBL results can be further used to generate fundamental solutions for two-dimensional non-gray radiative heat transfer in enclosures with arbitrary geometries.

While the current work is limited only to isothermal media, the solutions provide valuable benchmarks which can be used to validate approaches using other RTE solvers and differential spectroscopic models. Extension of the method to non-isothermal media will be the focus of future works.

4. Nomenclature

a	absorption coefficient, 1/m
A_i	area (i = 1,2), m^2
dA_i	differential area (i = 1,2), m^2
ds_1s_2	differential exchange factor between differential area dA_1 and finite area A_2, m^2
D	dimensional variables, m, Figs, 9a, 9b, 13a, 13b
E	error using a constant length scale to approximate the transmissivity between dA_1 and A_2, Eq. (12b)
F_{d1-2}	differential view factor between differential area dA_1 and finite area A_2
F_{1-2}	differential view factor between finite area A_1 and finite area A_2
L	pathlength, m
L_U	dimensional variables, Fig. 13a, 13b
L_L	dimensional variables, Fig. 13a, 13b
L_{pmb}	point mean beam length, m
$L_{pmb,o}$	optimal point mean beam length, m
L_{mb}	traditional mean beam length, m
$\vec{n}_i$	unit normal vector of surface i
R	radius of sphere (cylinder) in Fig. 1
$\vec{r}_i$	vector location of area dA_i
$\vec{r}_{ij}$	vector point from dA_i to dA_j
s_1s_2	exchange factor between finite area A_1 and finite area A_2, m^2
S_3	two dimensional integral function, Eq. (15)
S	error function used to determine OPMBL, Eq. (10a)
x	dimensional coordinate, Figs. 9a, 9b, 13a, 13b
y	dimensional coordinate, Figs. 9a, 9b, 13a, 13b
z	dimensional coordinate, Figs. 9a, 9b, 13a, 13b

subscripts

pp	parallel case
pd	perpendicular case

Greek Symbol

β	angular variable, Fig. 1
η	dimensionless variable, Eq. (21)
θ	angular variable, Fig.1
θ_c	angular variable of the spherical cap
θ_i	angular variable (i = 1, 2), Eq. (1)
θ_{d1-2U}	angle between dA_1 and the upper section of A_2, Fig. 8
θ_{d1-2L}	angle between dA_1 and the lower section of A_2, Fig. 8

τ_{d1-2} geometric mean transmittance between area dA_1 and A_2, Eq. (2)
τ_{1-2} geometric mean transmittance between area A_1 and A_2, Eq. (5)

5. Appendix

The mathematical development leading to the various PMBL and OPMBL expressions is presented in this Appendix.

5.1 Sphere

For the geometry as shown in Fig. 1 for the spherical system, the differential exchange factor between dA_1 and dA_2 is given by

$$ds_1 ds_2 = \frac{|\vec{r}_{21}\cdot\vec{n}_1||\vec{r}_{21}\cdot\vec{n}_2|}{\pi L^4} e^{-aL} dA_1 dA_2 \tag{A1}$$

with $\vec{n}_1$ and $\vec{n}_2$ being the normal vector of area dA_1 and dA_2 defined as

$$\vec{n}_1 = (0,0,1),\ \vec{n}_2 = (-sin\theta cos\varphi, -sin\theta sin\varphi, -cos\theta) \tag{A2}$$

The location of dA_1 and dA_2 expressed in a vector notation are

$$\vec{r}_1 = (0,0,-R), \vec{r}_2 = (Rsin\theta cos\varphi, Rsin\theta sin\varphi, Rcos\theta) \tag{A3}$$

$\vec{r}_{21}$ is a vector originated from dA_1 to dA_2 given by

$$\vec{r}_{21} = \big(Rsin\theta cos\varphi, Rsin\theta sin\varphi, R(1+cos\theta)\big) \tag{A4}$$

Substituting Eqs. (A2), (A3) and (A4) into Eq. (A1) yields

$$ds_1 ds_2 = \frac{R^2(1+cos\theta)^2}{\pi L^4} e^{-aL} dA_1 dA_2 \tag{A5}$$

which is equivalent to Eq. (7) in the main text. L is the length of the vector $\vec{r}_{21}$ given by

$$L = |\vec{r}_{21}| = \sqrt{2R^2(1+cos\theta)} \tag{A6}$$

Substituting Eq. (A6) into Eq. (A5) and set

$$dA_2 = R^2 sin\theta d\theta d\varphi \tag{A7}$$

Eq. (A1) becomes

$$ds_1 ds_2 = \frac{dA_1}{4\pi} e^{-aR\sqrt{2(1+cos\theta)}} sin\theta d\theta d\varphi \tag{A8}$$

For A_2 being the upper spherical section with $0 < \theta < \theta_c$, Eq. (A8) can be integrated to yield

$$\frac{ds_1s_2}{dA_1} = -\frac{1}{2aR}\left[2e^{-2aR} - \sqrt{2(cos\theta_c + 1)}e^{-\sqrt{2(cos\theta_c+1)}aR}\right] + \frac{1}{2(aR)^2}\left(e^{-\sqrt{2(cos\theta_c+1)}aR} - e^{-2aR}\right) \quad \text{(A9)}$$

which is identical to Eq. (8).

5.2 Cylinder

Consider the geometry and coordinate system in Fig. 1 as that in a two-dimensional plane, the differential exchange factor is formally identical to the general expression shown in Eq. (A1). Choosing a coordinate system with dA_1 situated at the origin (0, 0, 0), the various vectors are modified for the 2D planar system as follow:

$$\vec{n}_1 = (0,0,1), \quad \vec{n}_2 = (sin\theta, 0, cos\theta) \quad \text{(A10)}$$

$$\vec{r}_1 = (0,0,0), \vec{r}_2 = (Rsin\beta, y, Rcos\beta) \quad \text{(A11)}$$

Note that dA_1 is a differential area at the y = 0 plane while dA_2 is a differential area at an arbitrary value of y. The vector $\vec{r}_{21}$ and the line of sight distance is given by

$$\vec{r}_{21} = (Lsin\beta, y, Lcos\beta) \quad \text{(A12)}$$

$$S = |\vec{r}_{21}| = \sqrt{L^2 + y^2} \quad \text{(A13)}$$

The directional cosine at the differential area dA_1 is

$$\frac{|\vec{r}_{21}\cdot\vec{n}_1|}{S} = \frac{Lcos\beta}{S} \quad \text{(A14)}$$

The directional cosine at the differential area dA_2 is

$$\frac{|\vec{r}_{21}\cdot\vec{n}_2|}{S} = \frac{L(sin\beta sin\theta + cos\beta cos\theta)}{S} \quad \text{(A15)}$$

Using the following expression for the differential area of dA_2,

$$dA_2 = dydl_2 \quad \text{(A16)}$$

where dl_2 is the width of the infinite strip corresponds to dA_2 measured relative to θ, the two-dimensional angular coordinate of the unit normal. The product of the directional cosine and differential area is

$$\frac{|\vec{r}_{21}\cdot\vec{n}_2|}{S}dA_2 = \frac{L(sin\beta sin\theta + cos\beta cos\theta)}{S}\ dydl_2 = \frac{L}{S}dydl_{2,n} \tag{A17}$$

with

$$dl_{2,n} = dl_2(sin\beta sin\theta + cos\beta cos\theta) = Ld\beta \tag{A18}$$

being the width of the infinite strip measured relative to β, the angular coordinate of the vector $\vec{r}_{21}$. The differential exchange factor becomes

$$ds_1 ds_2 = \frac{L^3\, cos\beta}{\pi\, S^4}e^{-aS}dA_1 d\beta dy \tag{A19}$$

Integrating over the y-direction yields

$$\frac{1}{\pi}\int_{-\infty}^{\infty}\frac{L^3}{S^4}e^{-aS}dy = \frac{2}{\pi}\int_{1}^{\infty}\frac{1}{\eta^3}e^{-aL\eta}\frac{d\eta}{\sqrt{\eta^2-1}} = S_3(aL) \tag{A20}$$

Substituting Eq. (A20) into Eq. (A19) leads to Eq. (18).

5.3 Slab

Using the geometry and coordinate system as shown in Fig. 13a, the exchange factor between dA_1 and dA_2 is given by

$$ds_1 ds_2 = \frac{D^2}{\pi S^4}e^{-aS}dA_1 dA_2 = \frac{D^2}{\pi S^4}e^{-aS}dA_1 dxdy \tag{A21}$$

with

$$S^2 = x^2 + y^2 + D^2 \tag{A22}$$

Integrating over the y-direction yields

$$\frac{1}{\pi}\int_{-\infty}^{\infty}\frac{D^2}{S^4}e^{-aS}dy = \frac{D^2}{(x^2+D^2)^{\frac{3}{2}}}S_3\left[a\sqrt{x^2+D^2}\right] \tag{A23}$$

For A_2 being a two dimensional area extended from x = 0 to x = L

$$\frac{ds_1s_2}{dA_1} = \int_0^{L/D} \frac{1}{(\eta^2+1)^{\frac{3}{2}}} S_3\left[aD\sqrt{\eta^2+1}\right]d\eta \tag{A24}$$

For dA_1 in the vertical position as shown in Fig. 13b, the exchange factor is given by

$$ds_1ds_2 = \frac{Dz}{\pi S^4} e^{-aS} dA_1 dA_2 = \frac{Dz}{\pi S^4} e^{-aS} dA_1 dz dy \tag{A25}$$

Following the same development, the exchange factor becomes

$$\frac{ds_1s_2}{dA_1} = \int_0^{L/D} \frac{\eta}{(\eta^2+1)^{\frac{3}{2}}} S_3\left[aD\sqrt{\eta^2+1}\right]d\eta \tag{A26}$$

6. References

1. H. C. Hottel and A. F. Sarofim, "Radiative Transfer," McGraw Hill, New York, 1967.
2. J. J. Nobles, "The Zonal Method: Explicit Matrix Relations for Total Exchange Areas", International Journal of Heat and Mass Transfer, Vol. 18, No. 2, pp. 261-269, 1975.
3. W. W. Yuen and E. E. Takara, "The Zonal Method, a Practical Solution Method for Radiative Transfer in Nonisothermal Inhomogeneous Media", Annual Review of Heat Transfer, Vol. 8, pp. 153-215, 1995.
4. Kumar, S., A. Majumdar, and C. L. Tien, "The Differential-Discrete-Ordinate Method for Solution of the Equation of Radiative Transfer," J. Heat Transfer, Vol. 112, No. 2, pp.424-429, 1990.
5. W. A. Fiveland and A. S. Jamaluddin, "Three Dimensional Spectral Radiative Heat Transfer Solutions by the Discrete Ordinate Method", Journal of Thermophysics and Heat Transfer, Vol. 5, No. 3, pp. 335-339, 1991.
6. Chiu, E. H., G. D. Raithby and P. M. J. Hughes, "Prediction of Radiation Transfer in Cylindrical Enclosures with the Finite Volume Method," J. Thermophysics and Heat Transfer, Vol. 6, No. 4, pp. 605-611, 1992.
7. Ratzel, A. and J. R. Howell, "Two-Dimensional Energy Transfer in Radiatively Participating Media with Conduction by the P-N Approximation," Proc. 1982 International Heat Transfer Conf., Vol. 2, pp. 535-540, Munich, Sept. 1982.
8. Bayazitoglu, Y., and J. Higenyi, "The Higher-Order Differential Equations of Radiative Heat Transfer: P-3 Approximation," AIAA Journal, Vol. 17, No. 4, pp. 424,431, 1979.
9. Y. Zhang, et. al., "Natural Element Method for Solving Radiative Transfer With or Without Conduction in Three-dimensional Complex Geometries," J. Quantitative Spectrosc. Radiat. Transf. Vol. 129, pp. 118-130, 2013.
10. Haji-Sheikh, A, "Monte Carlo Methods" in W. J. Minkowycz, E. M. Sparrow, G. E. Schneider, and R. H. Fletcher (Eds.) Handbook of Numerical Heat Transfer, pp. 673-722, Wiley Interscience, New York, 1988.
11. Howell, J. R., "The Monte Carlo Method in Radiative Heat Transfer," Journal of Heat Transfer, Vol. 120, No. 3, pp. 547-560, 1998.

12. J. T. Farmer, and J. R. Howell, "Monte Carlo Strategies in Radiative Heat Transfer in Participating Media", Advances in Heat Transfer, J. T. Hartnett and T. Irvine (Eds), Vol. 31, pp. 1-97, 2008.
13. D. K. Edward, "Molecular Gas Band Radiation," Advances in Heat Transfer, J. T. Hartnett and T. Irvine (Eds), Vol. 12, pp. 115-193, 1976.
14. Tiwari, S. N., "Band Models and Correlations for Infrared Radiation", in "Radiative Transfer and Thermal Control," Progress in Astronautics and Aeronautics Series, pp. 155-182, AIAA, 1976.
15. W.L. Grosshandler, RADCAL, A Narrow-Band Model for Radiation Calculations in a Combustion Environment, NIST-TN-1402, National Institute of Standard and Technology, April 1993.
16. Tang, K. C., and M. Q. Brewster, "K-Distribution Analysis of Gas Radiation with Nongray, Emitting, Absorbing, and Anisotropic Scattering," J. Heat Transfer, Vol. 116, No. 4, pp. 980-985, 1994.
17. H. Zhang, and M. F. Modest, "A multi-scale full-spectrum correlated-k distribution for radiative heat transfer in inhomogeneous gas mixtures," Journal of Quantitative Spectroscopy and Radiative Transfer, vol. 73, no. 2–5, pp. 349–360, 2002.
18. Modest, M. F., "The Weighted-Sum-of-Gray-Gases Model for Arbitray Solution Methods in Radiative Heat Transfer," J. Heat Transfer, Vol. 113, No. 3, pp. 650-656, 1991.
19. Denison, M. K. and B. W. Webb, "A Spectral Line-Based Weighted-Sum-of-Gray-Gases Model for Arbitrary RTE Solvers," J. Heat Transfer, Vol. 115, No. 4, pp. 1004-1012, 1993.
20. C. Yin, L. C. R. Johansen, L. A. Rosendahl, and S. K. Kr, "New weighted sum of gray gases model applicable to computational fluid dynamics (CFD) modeling of oxy-fuel combustion: Derivation, validation, and implementation," Energy & Fuels, vol. 24, pp. 6275–6282, 2010.
21. J. T. Pearson, B. W. Webb, V. P. Solovjov and J. Ma, "Updated Correlation of the Absorption Line Blackbody Distribution Function for H2O Based on the HITEMP2010 Database,", J. Quant. Spectrosc. Radiat. Transfr., Vol. 128, pp. 10-17, 2013.
22. H. Amiri, K. Lari, P. J. Coelho, "Comparison of CK Model and Line by Line Model using Old and Updated Parameters/Database", International Journal of Thermal Sciences, Vol. 118, pp. 448-460, 2017.
23. Stone, P. H. and J. E. Gaustad, "The Application of a Moment Method to the Solution of Non-Gray Radiative Transfer Problems," Astrophysics J., Vol. 134, No. 2, pp.456-468, 1961.
24. P. J. Coelho, "Numerical Simulation of Radiative Heat Transfer from Non-Gray Gases in Three-Dimensional Enclosures," Journal of Quantitative Spectroscopy and Radiative Transfer, Vol. 74, pp. 307-328, 2002.
25. H. Amiri, P.J. Coelho, Natural element method for NON-GRAY radiation heat transfer problems, Int. J. Therm. Sci. 95 (2015) 9–20.
26. H. Amiri and K. Lan, "Line by line benchmark solutions for radiative heat transfer in 2D irregular enclosures with non-gray media", Int. J. Therm. Sci. 133 (2018) 307-319.
27. H. Chu, F. Liu, H. Zhou, "Calculations of gas radiation heat transfer in a two-dimensional rectangular enclosure using the line-by-line approach and the statistical narrow-band correlated-k model", Int. J. Therm. Sci. Vol. 59, pp. 66–74, 2012.

28. W. C. Tam, "Analysis of Heat Transfer in a Building Structure Accounting for the Realistic Effect of Thermal Radiation Heat Transfer," Ph.D. Thesis, The Hong Kong Polytechnic University (2013).
29. W. C. Tam, W. W. Yuen, "Assessment of Radiation Solver for Fire Simulation Models Using RADNNET-ZM", Proceeding of the Asia-Oceania Symposium on Fire Science, and Technology, pp. 113-126, Springer, Singapore, 2018.
30. D. B. Olfe, "Mean Beam Length Calculations for Radiation from Non-Transparent Gases", Journal of Quantitative Spectroscopy and Radiative Transfer, Vol. 1, pp. 169-176, 1961.
31. R. V. Dunkle, "Geometric Mean Beam Length for Radiant Heat Transfer Calculations", ASME Journal of Heat Transfer, Vol. 86, No. 1, pp. 75-80, 1964.
32. C. L. Tien and L. S. Wang, "On the Calculation of Mean Beam Length for a Radiating Gas," Journal of Quantitative Spectroscopy and Radiative Heat Transfer, Vol. 5, pp. 453-456, 1965.
33. D. A. Mandell, "Exact and Mean Beam Length Calculations for Radiative Heat Transfer in Gases," Combustion Science and Technology, Vol. 9, pp. 273-276, 1974.
34. A. T. Wassel and D. K. Edwards, "Mean Beam Length for Spheres and Cylinders," ASME Journal of Heat Transfer, Vol. 98, pp. 308-309, 1976.
35. A. D. Gosman and F. C. Lockwood, "Incorporation of a Flux Model for Radiation into a Finite Difference Procedure for Furnace Calculations," Proceedings of the 14th International Symposium on Combustion, The Combustion Institute, pp. 661-671. 1973.
36. F. Liu, H. A. Becker and Y. Bindar, "A Comparative Study of Radiative Heat Transfer Modeling in Gas-fired Furnaces Using the Simple Grey Gas and the Weighted-Sum-of-Gray-Gases Models", Int J Heat Mass Transfer, Vol. 41, pp. 3357-3371, 1988.
37. Fluent, A. N. S. Y. S. Ansys fluent theory guide. ANSYS Inc., USA, 15317, 724-746, 2011.
38. W. W. Jones, R. D. Peacock, G. P. Forney and P. A. Reneke, "CFAST: Consolidated Model of Fire Growth and Smoke Transport (Version 5), Technical Reference Guide," NIST-SP-1030, National Institute of Standard and Technology, October, 2004.
39. K. McGrattan, S. Hostikka, J. Floyd, H. Baum. and R. Rehm, "Fire Dynamics Simulator (Version 5), Technical Reference Guide," NIST Special Publication 1018-5, National Institute of Standard and Technology, October 1, 2007.
40. Gong, C., Ding, L., Wan, H., Ji, J., Gao, Z. and Yu, L., "Spatial temperature distribution of rectangular n-heptane pool fires with different aspect ratios and heat fluxes received by adjacent horizontal targets," Fire Safety Journal, 112, p.102959, 2020.
41. Kolstad, E.A., Frette, V., Krause, U. and Hagen, B.C., "Lip-height effect in diffusive pool fires," Fire Safety Journal, 125, p.103428, 2021.
42. W. W. Yuen and W. C. Tam, "Point Mean Beam Length, a New Concept to Enhance the Computational Efficiency of Multi-Dimensional, Non-Gray Radiative Heat Transfer", Numerical Heat Transfer, Part B: Fundamentals, DOI: 10.1080/10407790.2020.1819686.
43. W. W. Yuen and L. W. Wong, "Numerical Computation of an Important Integral Function in Two-Dimensional Radiative Transfer," Journal of Quantitative Spectroscopy and Radiative Transfer, Vol. 29, No. 2, pp. 145-149, 1983.

44. Yuen, W. W., "RAD-NNET, a Neural Network Based Correlation Developed for a Realistic Simulation of the Non-gray Radiative Heat Transfer Effect in Three-dimensional Gas-particle Mixtures." *International Journal of Heat and Mass Transfer*, 52, 3159–3168 (2009).

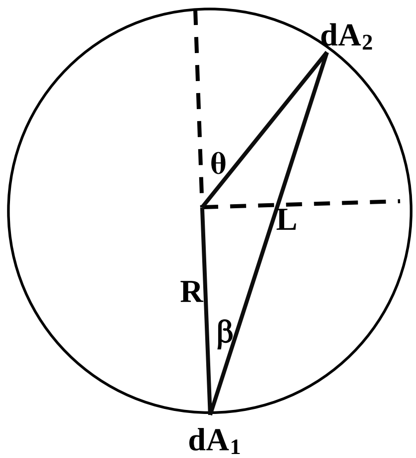

Figure 1: Geometry and coordinate system for a spherical system.

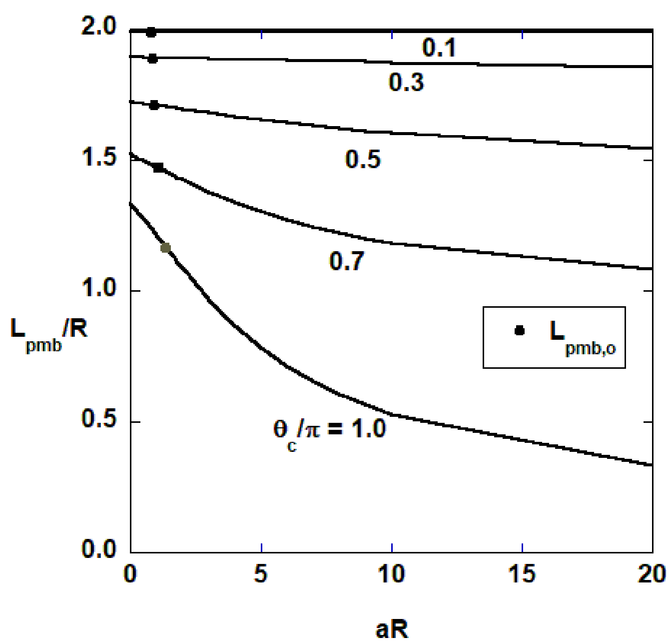

Figure 2: The effect of optical thickness (aR) on PMBL for radiative heat transfer to different sections of the surface of a spherical enclosure and the corresponding value of OPMBL.

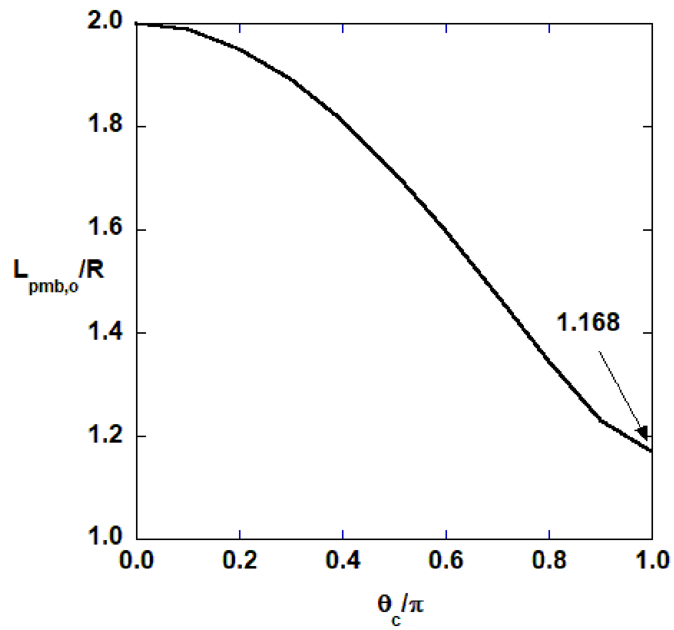

Figure 3: The OPMBL for the different upper sections of the surface of a spherical enclosure.

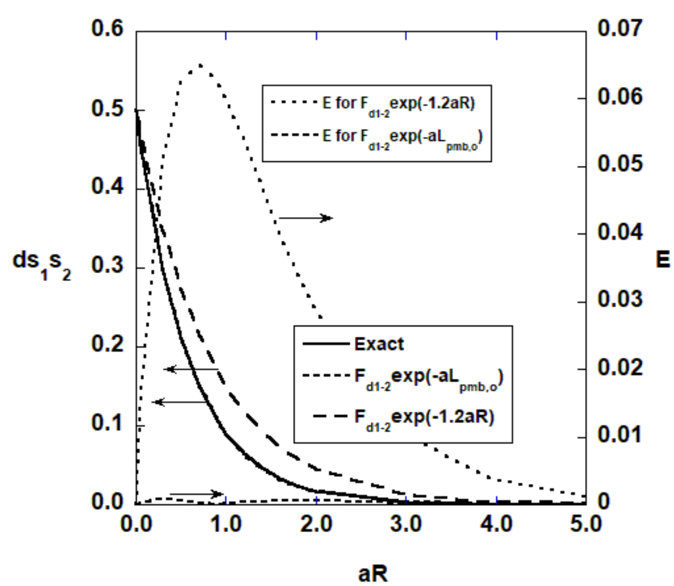

Figure 4: Comparison between the exact exchange factor (generated by direct integration) and approximate exchange factor generated by OPMBL and the error of the approximation for a section of the spherical surface with $\theta_c = \pi/2$ (note that the line for the exact solution of ds_1s_2 and the line for $F_{d1-2}exp(-aL_{pmb,o})$ are indistinguishable from each other).

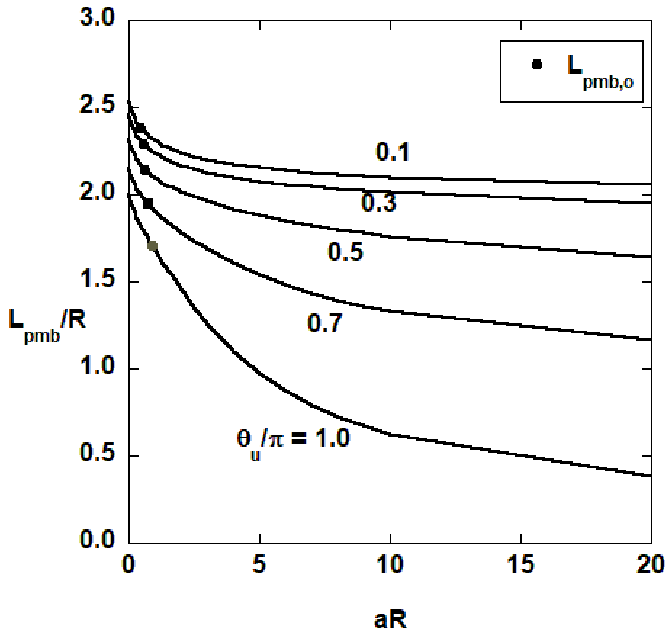

Figure 5: The effect of optical thickness (aR) on PMBL for radiative heat transfer to different sections of the surface of an infinite cylindrical enclosure and the corresponding value of OPMBL.

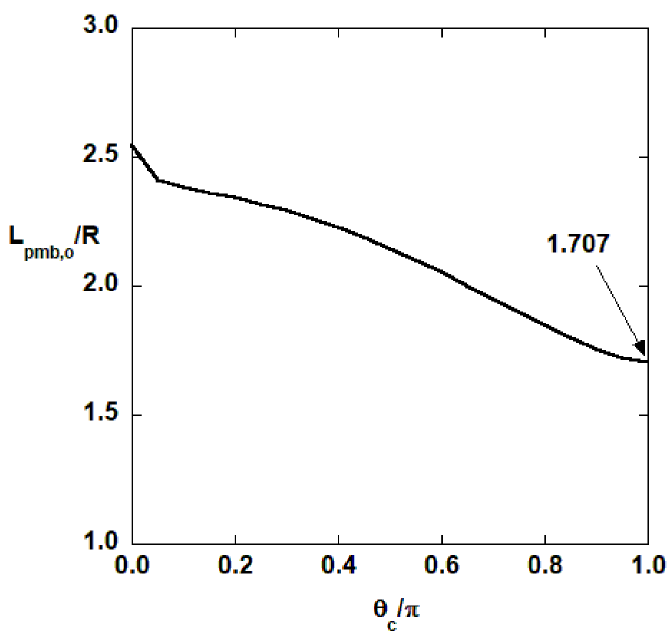

Figure 6: The OPMBL for the different sections of the surface of a 2D cylindrical enclosure.

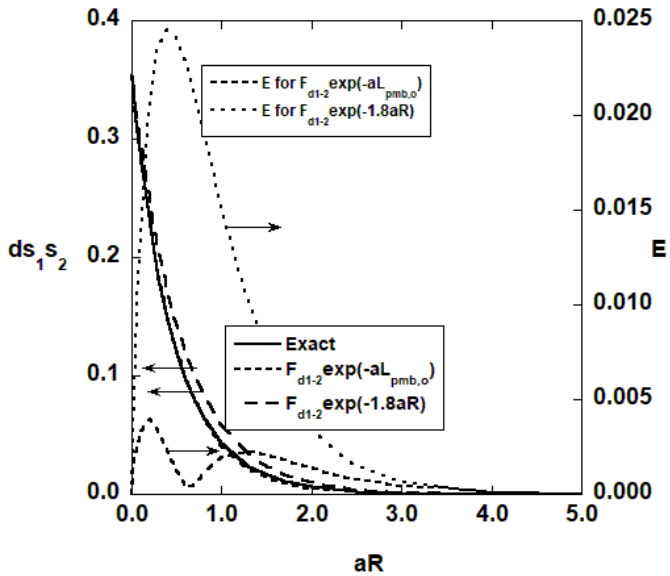

Figure 7: Comparison between the exact exchange factor (generated by direct integration) and approximate exchange factor generated by OPMBL and the error of the approximation for a section of the circular surface of an infinite cylinder with $\theta_c = \pi/2$ (note that the line for the exact solution of $ds_1 s_2$ and the line for $F_{d1-2}exp(-aL_{pmb,o})$ are indistinguishable from each other).

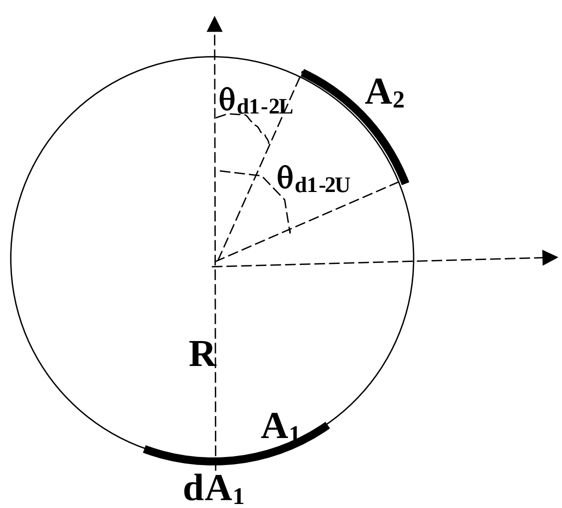

Figure 8: Geometry and coordinate system for the exchange factor between two finite circular arcs at the surface of an infinite cylinder.

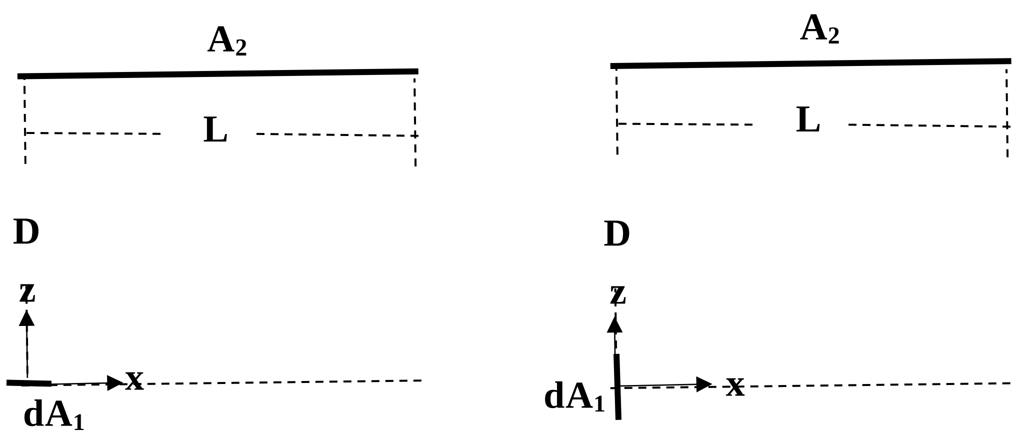

(9a) (9b)

Figure 9: Geometry and coordinate system for a 2D slab with a parallel dA_1 (9a) and perpendicular dA_1 (9b).

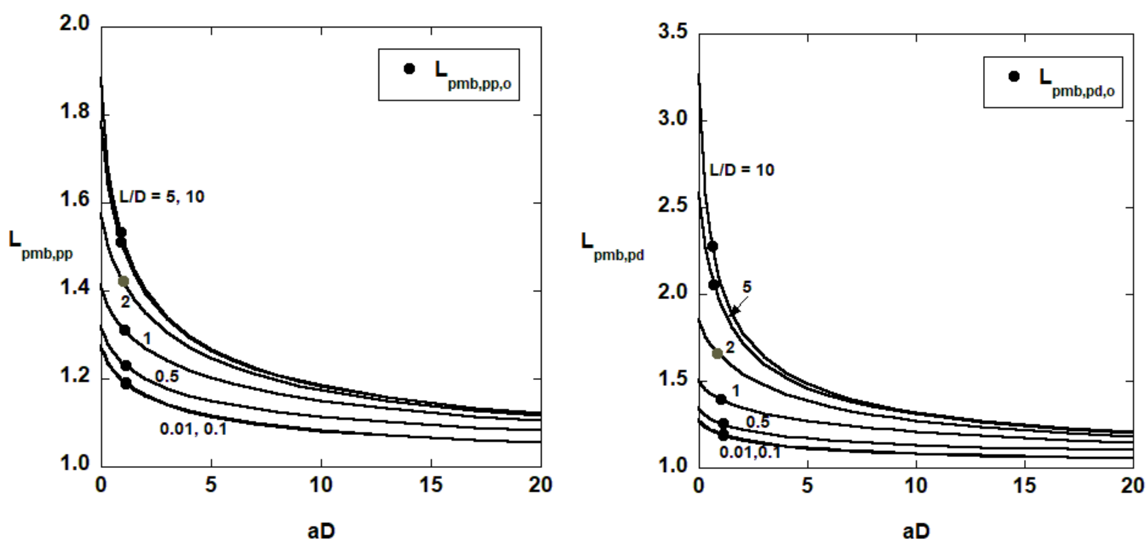

(10a) (10b)

Figure 10: PMBL for 2D slab with different L/D for the parallel dA_1 (10a) and perpendicular dA_1 (10b).

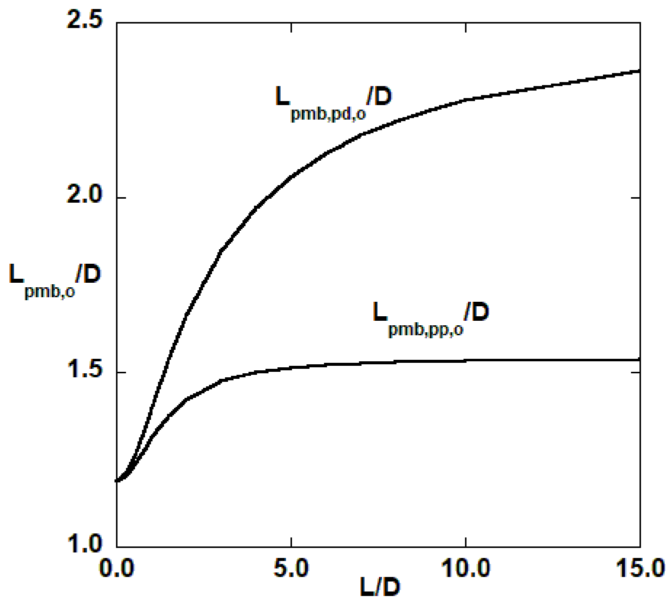

Figure 11: OPMBL for 2D slab with different L/D with a parallel *dA₁* ($L_{opmb,pp}$) and a perpendicular *dA₁* ($L_{opmb,pd}$).

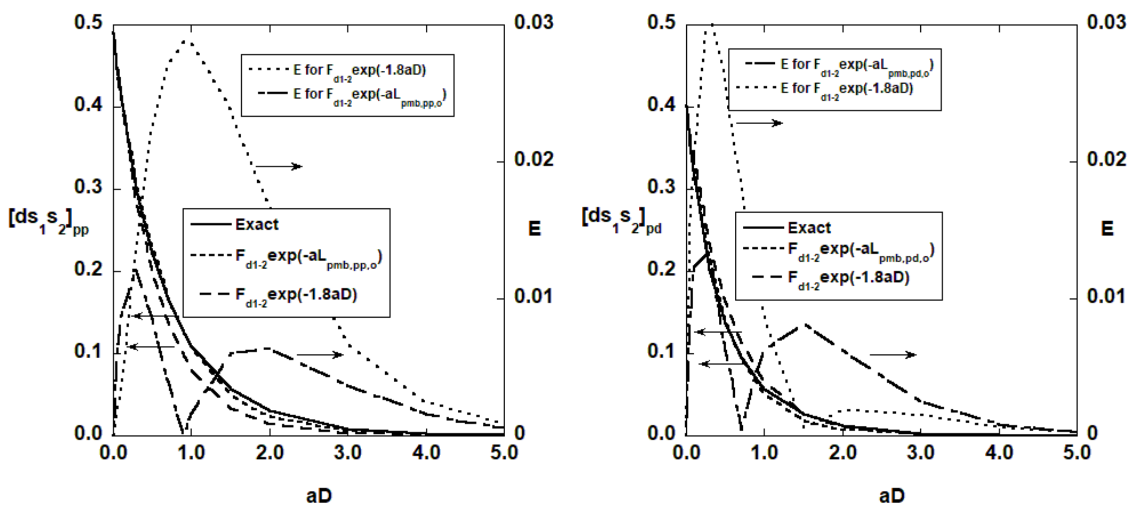

(12a) (12b)

Figure 12: Comparison between the exact exchange factor (generated by direct integration) and approximate exchange factor generated by OPMBL and the error of the approximation generated by the traditional MBL (1.8D) for a 2D slab with L/D = 5, a parallel *dA₁* (12a) and perpendicular *dA₁* (12b) (note that the line for the exact solution of ds_1s_2 and the line for $F_{d1-2}exp\left(-aL_{pmb,pp,o}\right)$ and the line for $F_{d1-2}\,exp\left(-aL_{pmb,pd,o}\right)$ are indistinguishable from each other).

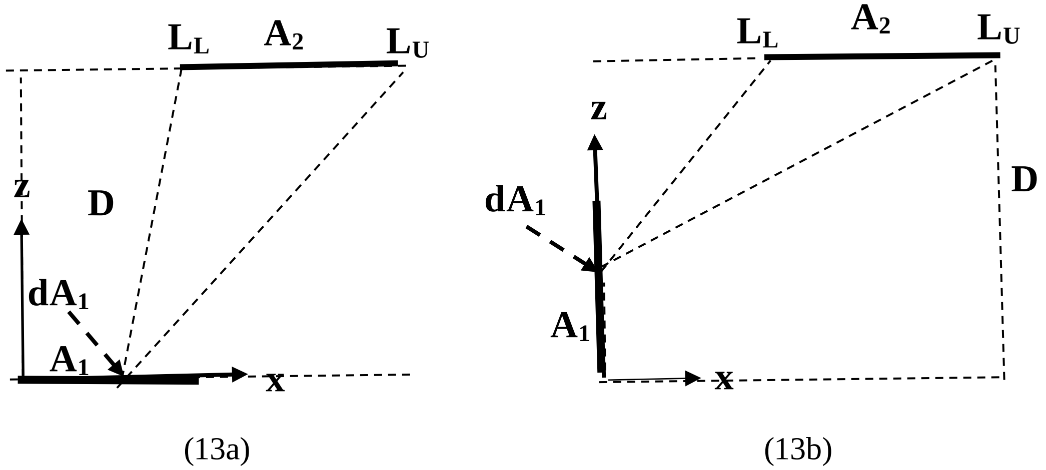

Figure 13: Geometry and coordinate system for the exchange factor between two finite 2D areas with a parallel (13a) or perpendicular (13b) orientation.